

Improved Heat and Particle Flux Mitigation in High Core Confinement, Baffled, Alternate Divertor Configurations in the TCV tokamak

Harshita Raj¹, C. Theiler², A. Thornton³, O. Février², S. Gorno², F. Bagnato², P. Blanchard², C. Colandrea², H. de Oliveira², B.P. Duval², B. Labit², A. Perek⁴, H. Reimerdes², U. Sheikh², M. Vallar², B. Vincent², the TCV Team², the Eurofusion MST1 Team⁶

¹*Institute for Plasma Research, Gandhinagar, India*

²*EPFL, SPC, Lausanne, Switzerland Ecole Polytechnique Fédérale de Lausanne (EPFL), Swiss Plasma Center (SPC), Lausanne, Switzerland*

³*CCFE, Culham Science Centre, Abingdon, Oxon, United Kingdom of Great Britain and Northern Ireland*

⁴*DIFFER-Dutch Institute for Fundamental Energy Research, Eindhoven, Netherlands*

⁵*See author list of H. Reimerdes et al. 2022 Nucl. Fusion 62 042018*

⁶*See author list of B. Labit et al 2019 Nucl. Fusion 59 086020*

Abstract

Nitrogen seeded detachment has been achieved in the Tokamak a Configuration Variable (TCV) in advanced divertor configurations (ADCs), namely X-divertor and X-point target, with and without baffles in H-mode plasmas with high core confinement. Both ADCs show a remarkable reduction in the inter-ELM particle and heat fluxes to the target compared to the standard divertor configuration. 95-98% of the peak heat flux to the target is mitigated as a synergetic effect of ADCs, baffling, and nitrogen seeded detachment. The effect of divertor geometry and baffles on core-divertor compatibility is investigated in detail. The power balance in these experiments is also investigated to explore the physics behind the observed reduction in heat fluxes in the ADCs.

1. Introduction

High particle and heat fluxes deposited in a narrow region at the divertor target challenges the operation of future tokamaks like ITER and DEMO[1,2]. If unmitigated, target heat fluxes would easily exceed material limits of $\sim 10\text{MW}/\text{m}^2$ [3]. Detached divertor operation [4–6], where a large fraction of the divertor power is dissipated through impurity radiation, plasma–neutral interactions, and volumetric recombination, is the key to steady-state plasma exhaust in future tokamaks. The detachment process typically sets in at target plasma temperatures below $\sim 5\text{eV}$ [7–9] and results in a reduction of target heat flux, temperature, and ion flux which is important to reduce target erosion [10]. Detachment can be attained by increasing separatrix density [7,12–14] or by impurity seeding [11,15,16]. The latter is predicted to be necessary in a reactor, due to confinement degradation at high upstream density [17] and the Greenwald density limit [18]. It is usually found that divertor detachment degrades the plasma confinement, as the detachment front cools the core plasma through degrading the H-mode pedestal [16,19–22]. To avoid core degradation, ITER plans to operate with a partially detached divertor [23,24], where only the portion of the strike point close to the separatrix is detached [19].

Minimizing any adverse impact on the core confinement while improving the detached operation regime is challenging but crucial in obtaining reliable power exhaust solutions for

future reactors. Recent DIII-D experiments, demonstrating fully detached divertor plasmas sustained with high core confinement [25], were a step forward towards this goal. Despite a degraded pedestal associated with divertor detachment, improved core-edge integration was attained by a self-organized plasma state with a low pedestal and a strong ITB, which improved the core confinement [25]. In AUG, real-time control of the X-point radiator with nitrogen seeding facilitated fully detached operation [26] with $\sim 95\%$ dissipation of the total power entering the divertor. An ELM-suppressed regime was also observed at a certain height of the radiator above the X-point, with minimal reduction of confinement, combining key requirements for a reactor.

Nevertheless, in DEMO, the exhausted thermal power from the main plasma to the scrape-off layer (SOL) is expected to be 150–300 MW, that is about 1.5–3 times higher than predicted in ITER (~ 100 MW) [27]. Achieving detached H-mode operation in DEMO will thus be considerably more challenging than for ITER [28,29]. Intense impurity seeding levels are expected to achieve the radiated power fraction of $\sim 95\%$ needed to reach detachment in such conditions, which may be seriously detrimental to the core plasma. In addition, the first wall in DEMO will be considerably more fragile than in ITER due to the tritium breeding structures [30]. A reliable heat exhaust solution for future reactors like DEMO may require alternative divertor concepts that cannot be tested in the conventional divertor used for ITER [31,32]. Exploration and assessment of alternative concepts, in parallel and with reference to the conventional divertor program in ITER, is needed to ensure the timely progress in exhaust solutions for DEMO and future reactors [28,32]. Alternative concepts include Alternative Divertor Configurations (ADCs) employing complex divertor geometries [31,33–35] and/or liquid metal divertor targets [36]. Increasing divertor baffling also offers cooler divertor conditions and promotes access to detachment [37,38]. ADCs aim to reduce the power and particle loads to the target by i) increasing the volume of the radiative region in the SOL and divertor, thereby increasing the dissipated power, ii) extending the wetted area by increased cross-field transport, e.g., through increased turbulence, and iii) enhancing positional stability of the detachment front e.g., by flaring of the flux surfaces in front of the target. Amongst today's most promising ADCs are: the X-Divertor (XD) [39–41] with large poloidal flux expansion (f_x) at the outer strike point (OSP), the X-Point Target (XPT) [42] geometry with a secondary X-point near the target, resulting among others, to a large connection length (L_{\parallel}), the Super-X divertor (SXD) with large total flux expansion [43], and the Snowflake divertor (SF) with an additional X-point close to the primary one [44,45]. Unique shaping capabilities of TCV's generous poloidal magnetic field array, and wide divertor diagnostic coverage [46] makes it particularly suitable for exploring the behavior of a range of ADCs with an immediate comparison to a similarly shaped conventional single null (SN) configuration at a proof-of-principle level.

Divertor detachment has been studied in TCV in L-mode confinement, single null configurations [15,47], and for several ADCs: the SF [44,48], XD [34,49], SXD [34], and XPT [34]. An increasingly pronounced roll-over in ion flux at the divertor targets, indicating deeper detachment, and lower peak parallel ion saturation currents as compared to SN were observed in XD configurations. However, the detachment threshold was not strongly affected by f_x [34]. A reduced radiation region location sensitivity to line average density was also observed in the

XD which is crucial for stronger detachment control. The decrease in the detachment threshold with increasing L_{\parallel} in XPT, as predicted by models, were not observed in TCV [34]. SOLPS-ITER simulations for the SN and XD in DIII-D suggest that the XD achieves an order of magnitude higher carbon emissivity than the SN due to stronger non-coronal effects at smaller field angles [50]. These non-coronal effects are even higher at higher input power leading to lower detachment thresholds in XD, which has been also experimentally observed on DIII-D [41]. Detachment in ELMy and ELM-free H-mode in ADCs were also studied in TCV [51]. A ~ 3 -4 times reduction in peak electron temperature and a ~ 2 times reduction in the total power load to the outer divertor between ELMs was observed with seeding, whereas the density profile remained broadly unaltered. The impurity emission front comparisons did not reveal any clear increase in divertor cooling in the XD. The back-transition of H-mode to L mode and a shorter H-mode phase caused by strong fueling and seeding were ascribed as the main obstacles in achieving higher divertor heat and particle flux mitigation in H-mode. The recent plasma exhaust (PEX) upgrades at TCV included new in-vessel divertor baffles [38], further diagnostic coverage and increased neutral beam heating capacity [52], improving the access to carry out proof-of-principle experiments of ADCs in H-mode. Models and experimental data from DIII-D indicate that increasing f_x and flaring should work in tandem with divertor closure to achieve a lower detachment threshold [41]. Experiments with baffles in TCV have shown easier access to detachment in L-mode [38] as well as improved core performance at high divertor neutral pressures in H-mode [53]. The exploration and assessment of the combined effect of baffling and ADCs in stable detached ELMy H-mode plasmas is the next logical step in developing advanced exhaust solutions in TCV and is the focus of this paper. Such studies can provide information on configuration(s) with the most promising core-divertor integration for further testing in the Divertor Tokamak Test facility (DTT), which is currently being designed to investigate alternative power exhaust solutions in DEMO-like conditions [54].

In this paper, we present results from N_2 seeded detachment experiments achieved in long-legged ADCs, namely the XD and the XPT, and compare them with the SN in stationary ELMy H-mode plasmas with and without divertor baffles for different NBI power levels (P_{NBI}). Here, the term ADCs will refer to both the XD and XPT. In particular, a ~ 2 -fold improvement in the inter-ELM heat and particle flux mitigation at the outer divertor with the same amount of N_2 seeding in the ADCs in comparison to the SN was achieved, while simultaneously maintaining high core confinement.

The rest of this paper is structured as follows: in section 2 an overview of the experiments and key diagnostics important for this study are described. In section 3, detachment with high core confinement in the baffled ADCs and SN is demonstrated. In section 4, the effect of geometry on target ion flux profiles and integral values in attached and detached phases are presented. In section 5, the effect of geometry on target heat flux profiles is discussed and compared with the effect of baffles. In section 6, the effect of geometry and baffles on the radiated power distribution is presented. In addition, the power balance in the ADCs and the SN is compared with the goal of explaining the physics behind the observed improvement in the exhaust performance of the ADCs. Finally, in section 7, the key results from these experiments are summarised and motivation for future experiments is discussed.

2. Experiment overview

These experiments are carried out at the TCV tokamak, which is a carbon walled, medium-sized tokamak (major radius, $R_0=0.88$ m, minor radius, $a=0.25$ m) with unique flexibility to vary the plasma shape, using 16 independently controlled poloidal field coils [46,52,55]. Figure 1, a)-c), shows the poloidal magnetic geometry of the SN (in red), the XD (in blue), and the XPT (in green) along with radial profiles of their f_x and L_{\parallel} in d) and e) respectively. In this paper, the term SP2-XPT and SP4-XPT will be used to denote the OSP on the high field side and low field side of the XPT geometry respectively, as marked in figure 1(c). In the XPT, the distance between the two X-points mapped upstream (dr_{X2}) is less than 2 mm, i.e., much smaller than the heat flux decay length, λ_q (~ 5 mm).

We start from ELMy (Type I) H-mode plasmas similar to those presented in [53] with a plasma current (I_p) = 170 kA, toroidal magnetic field (B_0) = 1.4 T, neutral beam heating power

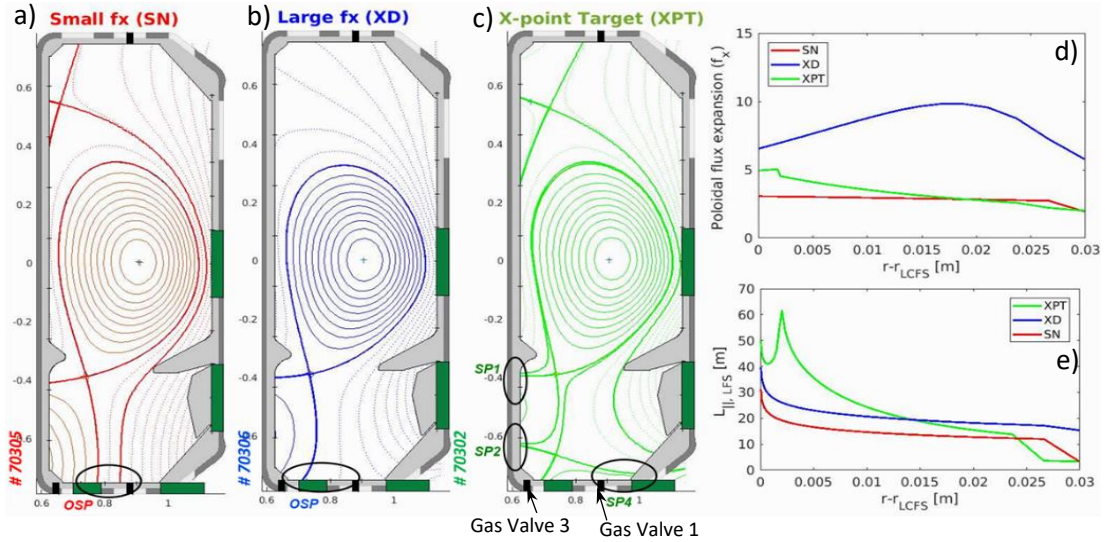


Figure 1: Plot showing poloidal magnetic geometry of (a) the SN (red), (b) the XD (blue), and (c) the XPT (green) and their radial profile of d) f_x and e) L_{\parallel} are plotted on the right top and bottom respectively.

(P_{NBI}) of 0.75 MW or 1.3 MW, $q_{95} \sim 5$ and a Greenwald density fraction $f_G \sim 0.55$. Plasmas in both ADCs and the SN were repeated with and without the polycrystalline graphite baffles recently installed in TCV. The B_0 direction is such that the ion grad B-drift is directed downwards, favorable for H-mode access. I_p is in the same direction. These are Deuterium discharges, fuelled from gas valve 1 present at the bottom of the TCV vessel (see fig.1). Detachment is achieved by injecting a prescribed nitrogen gas (N_2) pulse from gas valve 3, also situated at the bottom but at the high field side (figure 1). These are piezo-electric gas valves with an integrated pressure sensor, that provides calibrated flow rates into TCV [34]. Density (n_e) and temperature (T_e) profiles are obtained from Thomson spectroscopy [56] viewing the plasma core and pedestal. The plasma parameters at the divertor targets are measured using an extensive array of wall-embedded Langmuir Probes (LPs) [57,58]. They are operated with a triangular voltage sweep, ranging from -120V to +80 V, at a frequency of 990 Hz. Details on the LP analysis can be found in Ref [57]. The newly installed RADCAM system with five camera modules containing gold foil bolometers with 120 line of sights have been used to

estimate the radiated power and its spatial distribution [59]. The line integrated chord intensities thus obtained are tomographically inverted using a minimum Fisher regularization method [60]. MANTIS (Multispectral Advanced Narrowband Tokamak Imaging System) [61] captures images from the divertor region that are inverted using the CalCam package to obtain 2D poloidal maps of the emissivity of the selected radiation lines. In this paper, we will focus on CIII (465.8 nm) line emissivity profiles. A “CIII-front” can be defined as the position where the emissivity along the outer divertor leg decreases by 50% [34,51].

3. Divertor detachment in high core confinement, baffled ADCs

Detached ELMy H-mode with high core confinement is achieved with N_2 seeding in ADCs and SN geometries with and without baffles in TCV for a range of input powers. The H98 scaling factor is used to assess core performance [62]. It is defined as the ratio of the experimental confinement time (τ_E) and the ITER-98P(y,2) confinement time scaling law (τ_E^{IPB98}), given as

$$\tau_E^{IPB98} = 0.0562 I^{0.93} B^{0.15} n^{0.41} P^{-0.69} R^{1.97} \kappa^{0.78} \epsilon^{0.58} M^{0.19}$$

where I (MA) is the plasma current, B (T) is the toroidal magnetic field, n (10^{19} m^{-3}) is the line averaged density, P (MW) the input power, R (m) the major radius, κ the plasma elongation,

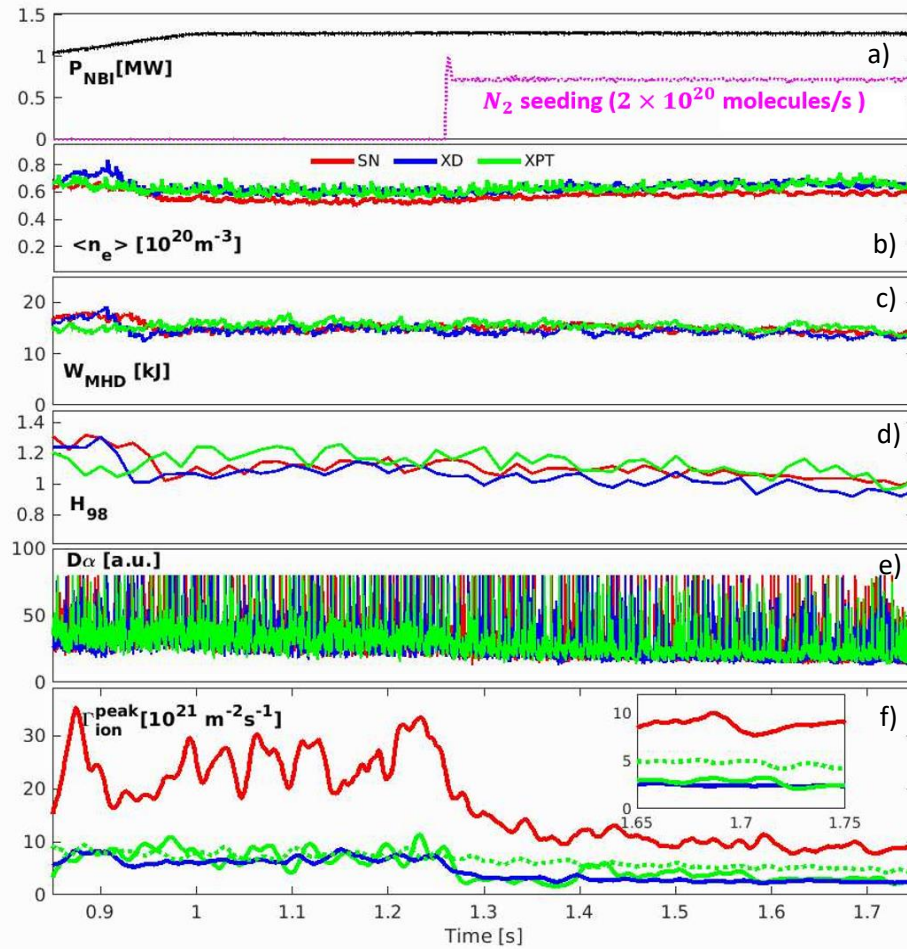


Figure 2: Plots showing time traces of a) NBI power (black), N_2 pulse (magenta), b) line average density, c) stored energy, d) H_{98} factor, e) D_α line emission intensity and f) peak parallel ion flux at OSP for SN (red), XD (blue) and XPT (green).

ε is the inverse aspect ratio, and M ($\sim m_i/m_p$) is the hydrogen isotope mass ratio. τ_E is calculated as $\frac{W_{MHD}}{P_{in}}$, where P_{in} is the input power to the plasma and W_{MHD} the stored plasma thermal energy. W_{MHD} is calculated using electron and ion density and temperature profiles from Thomson spectroscopy and CXRS, respectively. The W_{MHD} thus calculated has also been verified with W_{MHD} obtained from a diamagnetic loop.

Figure 2 shows some major plasma parameters of high power ($P_{NBI} = 1.3 MW$) baffled shots in ADC and SN geometry with high core confinement ($H_{98} \geq 1$) and stable detached divertor conditions that last for at least 0.4s following the N_2 injection. NBI starts at 0.8s, pushing the plasma into H-mode and each geometry stays in a stable ELMy H-mode until the end of the NBI pulse at 1.8s. A constant N_2 seeding pulse is applied from 1.25s until the end of discharge. Similar core (line-average) density is maintained in each geometry (fig. 2b) with similar fueling conditions. Before N_2 seeding, high core confinement with $H_{98} = 1 - 1.2$ is obtained in each geometry, that decreases slightly following the N_2 injection. H_{98} remains ≥ 1 till the end of the detached H-mode phase, indicating sustained high core confinement (fig 2d). Similar H_{98} factors and W_{MHD} during attached and detached H-mode (fig 2c-d) in both the ADCs and the SN suggests a weak influence of geometry on core confinement. The inter-ELM peak ion flux at the OSP ($\Gamma_{ion,OSP}^{peak}$) obtained using LPs (fig 2f) sharply decreases after N_2 injection in each geometry, indicating divertor detachment. Both ADCs exhibit 50-70% lower $\Gamma_{ion,OSP}^{peak}$ in the attached, as well as detached phase, compared to the SN geometry, while, as noted already, maintaining similar core confinement. During the attached phase, $\Gamma_{ion,OSP}^{peak}$ in the XD and both active OSPs of the XPT (SP2-XPT, SP4-XPT) appear quite similar. The effect of N_2 seeding on the peak flux at SP4-XPT is weaker as compared to SP2-XPT and the XD, that exhibit the lowest particle fluxes in the detached phase. However, despite weaker detachment at SP4-XPT, its Γ_{ion}^{peak} is half of that in the SN. Detailed discussion on the effect of geometry and baffles on particle and heat fluxes at the target will be presented in section 4.

3.1 Effect of geometry on core/pedestal

The effect of divertor geometry on the pedestal profiles was probed by comparing the pedestal n_e , T_e and P_e profiles obtained from TS as presented in fig 3(a-c) in the attached and 3(d-f) in the detached phase. These profiles are obtained from the [0.3-0.9] fraction of the ELM cycle.

Normalized poloidal flux, $\rho_\psi = \sqrt{\frac{\psi - \psi_0}{\psi_{x1} - \psi_0}}$, (where ψ is the poloidal flux and ψ_0 and ψ_{x1} its values at the magnetic axis and primary X-point, respectively) is used as the radial coordinate. Although the H_{98} factor and W_{MHD} seem largely unaffected by the divertor geometry, the pedestal n_e , T_e and P_e profiles obtained during inter-ELM time windows show marginally higher $n_{e,ped}$, $T_{e,ped}$ and $P_{e,ped}$ in the ADCs, especially for the XPT compared to the SN in both the attached and detached phases.

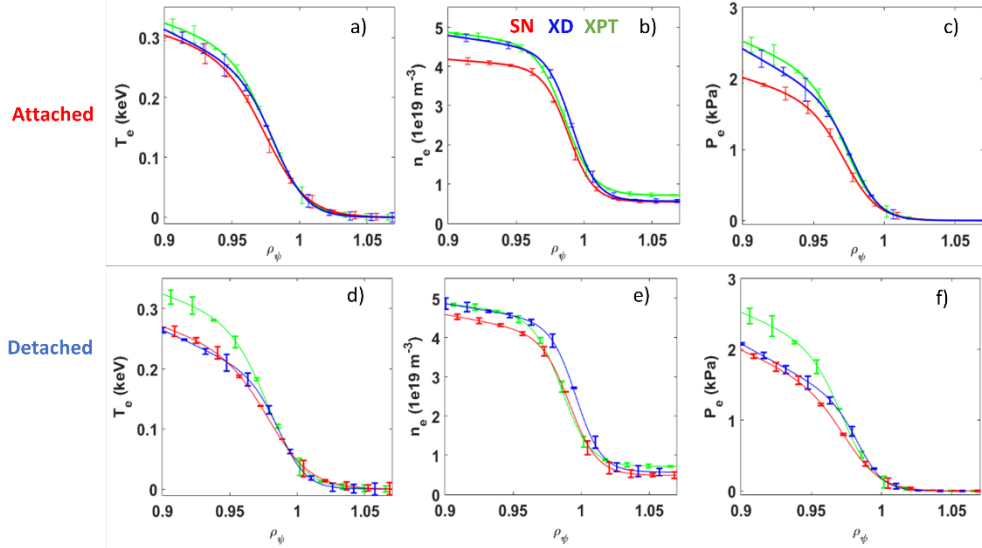


Figure 3: Plots showing radial inter-ELM pedestal profiles of T_e , n_e and P_e in (a-c) attached and (d-f) detached phase, respectively.

A minor degradation in the $n_{e_{ped}}$ and $T_{e_{ped}}$ is observed in the detached phase in all geometries, which is consistent with the H98 and W_{MHD} trends discussed earlier. It is worth mentioning that although the H98 and W_{MHD} slightly decrease following N2 seeding, the core density increases in all three geometries, as shown in figure 4a.

The effect of geometry on core confinement and pedestal parameters in ADCs was further examined at lower power, $P_{NBI} = 0.75 \text{ MW} - 1 \text{ MW}$, here again, with and without baffles,

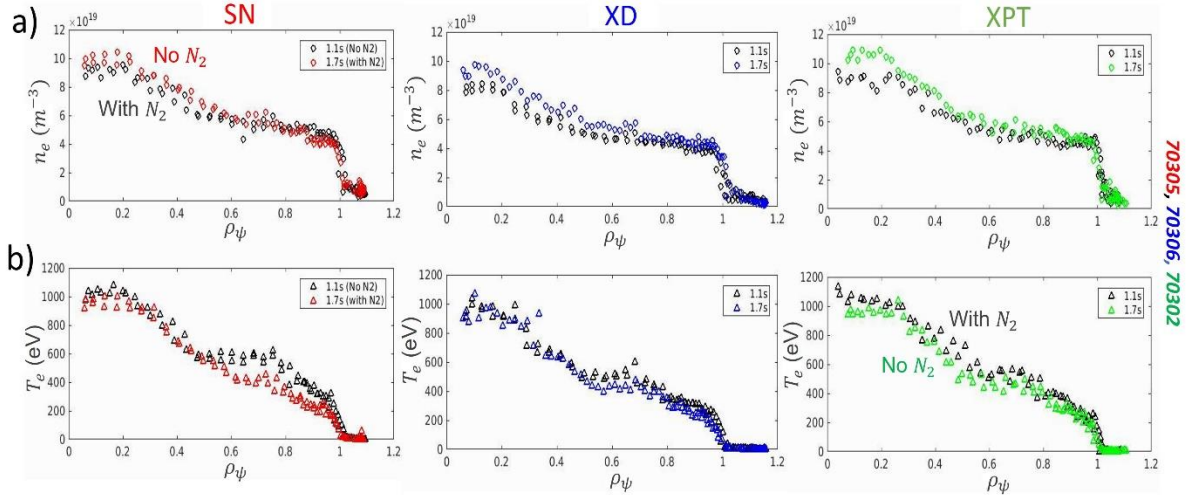


Figure 4: Plots showing radial profiles of a) n_e and b) T_e in SN, XD and XPT respectively. Black points show the attached, and coloured points show the detached phase. (Same shots as in fig.3)

and showed similarly small dependencies. The ELM behaviour is another important aspect of H-mode plasmas, as it plays a significant role in the power balance. As we report upon the inter-ELM power and particle exhaust in the following sections, we shall also report on the ELM behaviour changes with the divertor geometry. Figure 5 shows the ELM frequency (f_{ELM}), energy lost per ELM (dW_{ELM}) and ELM power loss (P_{ELM}) for the 1.3 MW baffled shots presented in figure 1 and 2. dW_{ELM} is estimated as the difference in the stored energy,

from a diamagnetic loop before and after an ELM following correction of any over-shoot in that measurement [51].

P_{ELM} is estimated as the product of the energy loss per ELM and the ELM frequency ($P_{ELM} = f_{ELM} \cdot dW_{ELM}$). As indicated by figure 5, in the attached phase, f_{ELM} and P_{ELM} is not strongly affected by the divertor geometry, although f_{ELM} is somewhat lower and dW_{ELM} higher in the XPT. From the start of the seeding phase, f_{ELM} increases and dW_{ELM} decreases. By the end of the seeded phase, dW_{ELM} has decreased by 35-40% in all geometries. Despite some variability in f_{ELM} and dW_{ELM} , P_{ELM} is similar in all the geometries, dropping by ~30% due to seeding. Unlike AUG experiments [63], where an ELM-suppressed regime is observed at a certain height (~10 cm) of the XPR above the X-point, discharges reported in this paper remain in an ELM regime in all geometries. The decreasing dW_{ELM} and P_{ELM} and increasing ELM frequency indicate, however, a tendency towards a small ELM regime late in the detached H-mode phase.

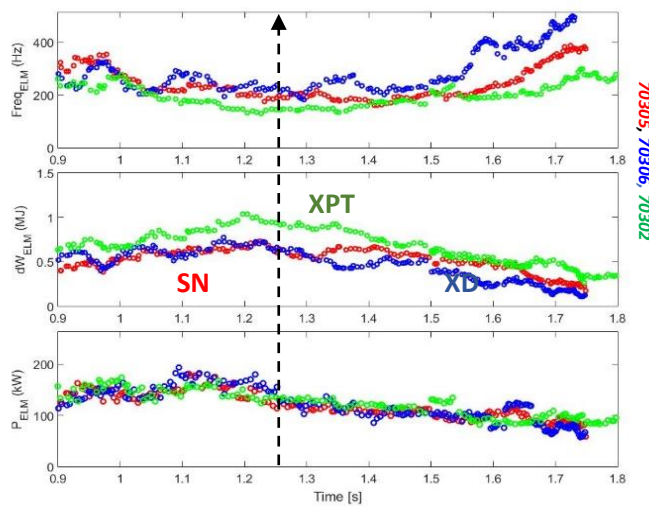


Figure 5: Plots showing the time evolution of the 20 points moving average of a) f_{ELM} , b) dW_{ELM} and c) P_{ELM} in SN (red), XD (blue) and c) XPT (green) in 1.3 MW plasmas with constant N₂ seeding starting at 1.25s, indicated by dotted black arrow.

3.2 Detachment in all geometries verified with MANTIS

Earlier detachment studies [15,34,51,64] showed that the CIII front is a good proxy for the position of the boundary of the cold radiative region along the divertor leg. The displacement of this CIII-front from the target to the X-Point is indicative of divertor cooling, and, thereby,

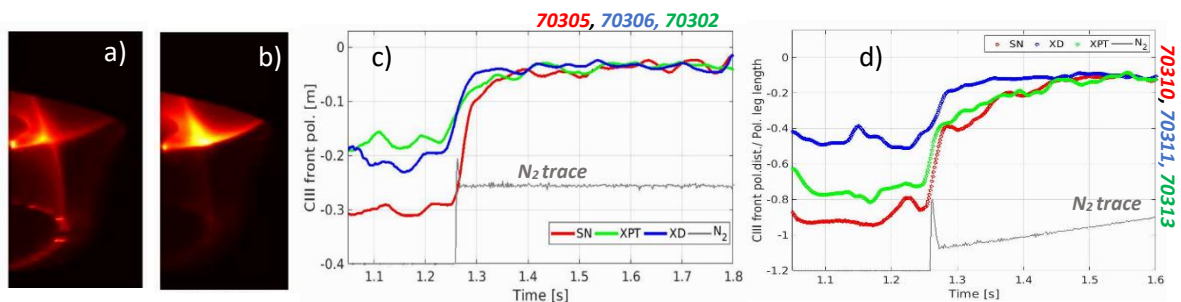


Figure 6: Inter-ELM MANTIS time frame from the SN captured during a) the attached phase and b) detached phase. Plot showing temporal evolution of the inter-ELM (c) poloidal distance of CIII front to the primary X-point and d) CIII front poloidal distance normalized w.r.t the total poloidal leg length in 1.3 MW baffled ADCs and SN.

a marker for detachment. Figure 6 (a) shows an inter-ELM MANTIS time frame captured during the attached phase in the SN geometry, where the CIII emission extends along the entire outer divertor leg in contrast to the detached phase, where the CIII front is very close to the X-point in between ELMs (see fig 6 b). Figure 6(c) shows the temporal evolution of the inter-ELM poloidal distance of the CIII front to the primary X-point in 1.3 MW baffled ADCs and SN. A 25 ms median filter was used to obtain the inter-ELM CIII front of each geometry. During the attached phase, the CIII front sits closer to the primary X-point in the ADCs, compared to the SN, indicating colder divertor conditions in the ADCs. As the N_2 seeding starts, the CIII front migrates further towards the X-point in each geometry. These results from MANTIS confirm detachment is obtained for the ADCs and the SN. An advantage of ADCs in terms of divertor cooling is also apparent in a facilitated detachment onset. It should be noted that the poloidal leg length of the outer divertor, it should be noted, is different in each geometry. Therefore, the CIII front poloidal distance normalized w.r.t the total poloidal leg length ($CIII\ front_{NM}$) may be a more adequate parameter to compare. This is plotted in figure 6d for the ADCs and the SN in 1.3 MW baffled scenarios with a N_2 seeding ramp. In the attached phase, the $CIII\ front_{NM}$ is closest to the X-point in the XD, followed by the XPT and lastly, the SN geometry where the $CIII\ front_{NM}$ is close to the target. This indicates that between the two ADCs, the XD has a colder divertor in the attached phase.

Together with the LP data (fig.2), these results provide further evidence of the achievement of a stable N_2 seeded detached H-mode with high core confinement in the ADCs and the SN. We also presented indications of colder divertor conditions (from CIII front measurements) and lower target peak ion fluxes (fig 2f) in the ADCs. In the following sections, we further examine the LP data, quantifying the advantages of the ADCs over the SN in terms of the particle and heat fluxes on the divertor target.

4. Effect of geometry on target ion flux profiles

For a reliable interpretation of LP data, the inter-ELM data in swept mode is carefully extracted for each discharge, and then analysed to obtain target plasma parameters. The details on LPs in TCV and its data analysis are discussed in Ref [59]. Figure 7 shows the radial profiles of the inter-ELM ion flux parallel to the magnetic field (J_{sat}) measured at the OSP as a function of ρ_ψ for the SN (fig 7a) and the ADCs (fig.7 b, c, d) during the attached (black) and the detached phases (colored). In the attached H-mode phase, the XD, SP2-XPT and SP4-XPT exhibit

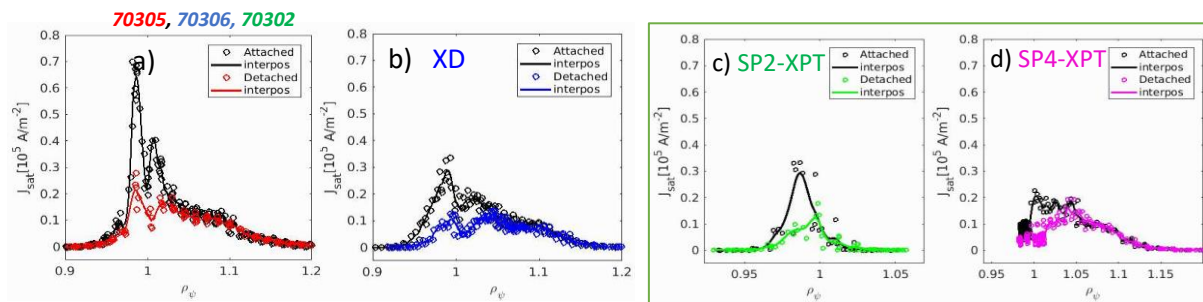


Figure 7: Plots showing the radial profiles of the inter-ELM ion current parallel to the magnetic field (J_{sat}) at the OSP vs. ρ_ψ for a) SN, b) XD, c) SP2-XPT and, d) SP4-XPT during the attached (black) and the detached phase (colored).

substantially (<50%) lower peak J_{sat}^{peak} at the OSP in comparison with the SN. The J_{sat}^{peak} in the XD and SP2-XPT are similar in magnitude, whereas the J_{sat}^{peak} at the SP4-XPT is substantially lower. This advantage of ADC over the SN in terms of lower peak ion fluxes also persists into the detached phase. The effect of seeding at SP4-XPT appears weaker than for the SP2-XPT.

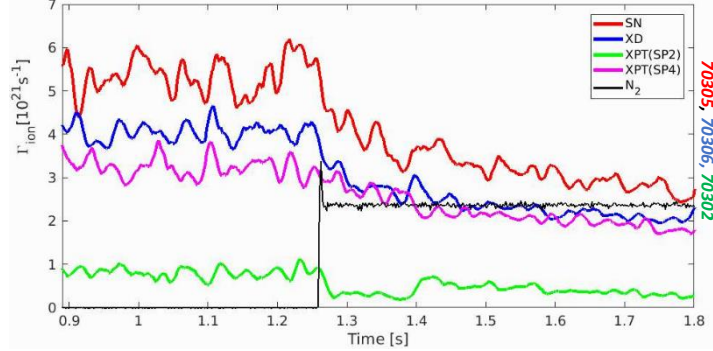


Figure 8: Plot showing time evolution of the integrated ion flux to the OSP in the SN (red), XD (Blue), SP2-XPT (green) and SP4-XPT (magenta)

This could be due to the proximity of SP2-XPT to the N₂ seeding gas valve (valve3) that is poloidally farther for SP4-XPT. To elucidate any issue of poloidal asymmetry in detachment in the XPT, N₂ seeding experiments with multiple poloidal gas valves are planned for future TCV experiments. They are expected to add further important details to the results presented here. Figure 8 show the integrated ion flux (Γ_{ion}) at the OSP in the SN and the ADCs. The total Γ_{ion} in the ADCs is lower than for the SN in both attached and detached phases. In all geometries, Γ_{ion} gradually decreases with N₂ seeding in the detached phase. It is worth noting that although Γ_{ion} at SP2-XPT is much lower than SP4-XPT, the J_{sat}^{peak} at SP2-XPT is similar due to the more peaked profile. We have shown that both ADCs demonstrate a clear advantage over the SN with lower J_{sat}^{peak} (fig 2f and 7) as well as lower Γ_{ion} (fig 8) at the OSP in H-mode. However, for attached XPT plasmas, these desirably low J_{sat}^{peak} at both SP2 and SP4 are limited to scenarios with extremely small dr_{X2} (~ 1 mm), i.e. $\sim 20\%$ of the (upstream) heat flux decay length λ_q (~ 5 mm), measured using IR in similar SN geometry. In high dr_{X2} scenarios, J_{sat}^{peak} SP2 is almost the same as in the SN, denoted by grey points in fig 9d and 9e. Again, a similar J_{sat}^{peak} distribution at SP2-XPT and SP4-XPT was obtained by carefully optimizing the distance between the X-points. Thus, as one might expect, the J_{sat}^{peak} ratio at SP2 and SP4 in the XPT geometry strongly depends on the distance between the X-points. Figure 9 (a) shows the distance between the X-points mapped upstream (dr_{X2}) for two XPT discharges with similar plasma parameters but different dr_{X2} . Figure 9 (b) and 9 (c) show the corresponding geometries. In figure 9 (d) and (e) we show the radial J_{sat} profile for SP2-XPT (magenta), SP4-XPT (blue) and compare them to the J_{sat} in the SN (grey) of the XPT discharges. With high dr_{X2} (5-7 mm), J_{sat}^{peak} at SP2 is as high as in the SN and J_{sat}^{peak} at SP4 is much lower. For smaller dr_{X2} (1-2 mm), J_{sat}^{peak} at SP2 and SP4 are comparable and considerably lower than for SN. From lower parallel particle fluxes in the ADCs reported here, we can also expect lower parallel heat fluxes, discussed in the next section.

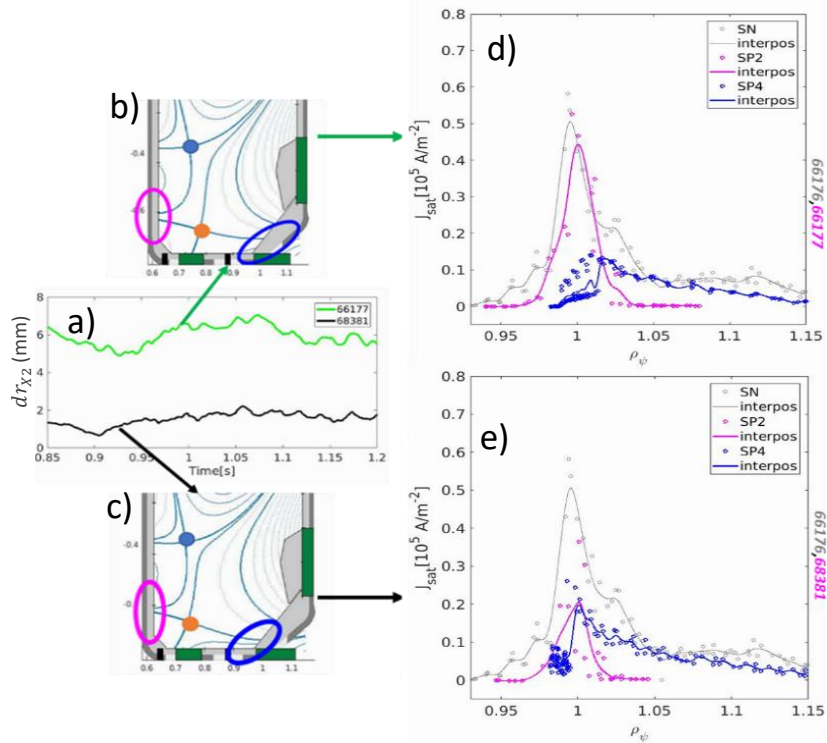


Figure 9: (a) Time evolution of dr_{X2} for two XPT discharges with similar plasma parameters with high dr_{X2} (green) and low dr_{X2} (black). 2D equilibrium showing both X-points for XPT with (b) high dr_{X2} and (c) low dr_{X2} . Radial J_{sat} profile of SP2-XPT (magenta), and SP4-XPT (blue) in (d) high dr_{X2} and (e) low dr_{X2} case, in comparison to the J_{sat} profile in the SN (grey).

5. Improved heat flux mitigation in baffled ADCs

5.1 Effect of ADCs & baffles on target heat flux

In supplement to the CIII front measurements indicating colder divertor conditions in the ADCs (section 3.2) and lower peak parallel ion fluxes (section 4), we present more detailed and qualitative evidence from the LPs showing improved heat flux mitigation in ADCs. The inter-ELM parallel heat fluxes at the OSP ($q_{||,OSP}$) is evaluated as $q_{||,OSP} = J_{sat} (\gamma T_e + E_{pot})$, where E_{pot} is the potential energy carried by the incident ions ($E_{pot} = 13.6 + 2.2 = 15.8$ eV, following Ref. [59]) and, γ is the sheath heat transmission coefficient, taken to be $\gamma = 5$. Experiments were performed to compare the impact of divertor geometry (XD and XPT) and baffles on peak heat flux mitigation. We will first discuss the impact of ADCs and baffles in the attached phase. Figure 10 shows the radial profiles of $q_{||,OSP}$ for the ADCs and the SN without baffles (top row) and with baffles (bottom row). The $q_{||,OSP}$ profiles plotted here are obtained from the attached H-mode phase in low power ($P_{NBI} = 0.75$ MW) plasmas. We note that here, $q_{||,OSP}$ is shown rather than the perpendicular heat flux to the wall, to avoid effects related to varying the magnetic field incidence angles at the target.

As expected from the J_{sat} profiles, the peak $q_{||,OSP}$ ($q_{||,OSP}^{peak}$) is highest in the unbaffled SN with $q_{||,OSP}^{peak} \sim 4$ MW/m². When increasing f_x (in unbaffled XD), $q_{||,OSP}^{peak}$ is reduced by $\approx 60\%$ reaching 1.6 MW/m². Conversely, with baffles (in baffled SN) one obtains $\approx 40\%$ lower $q_{||,OSP}^{peak}$, 2.5 MW/m². As a cumulative impact of baffled and increased f_x , $\approx 85\%$ $q_{||,OSP}^{peak}$

mitigation was achieved, with $q_{||,OSP}^{peak} \sim 0.6 \text{ MW/m}^2$. By adding a secondary X-point (unbaffled XPT), we could obtain $\approx 75\%$ lower $q_{||,OSP}^{peak}$ at both SP2 and SP4, provided that $dr_{X2} \leq 1 \text{ mm}$. $q_{||,OSP}^{peak}$ at SP2-XPT with high $dr_{X2} (\geq 2 \text{ mm})$ was found to be up to two times higher, but still lower than the SN despite similar J_{sat} (see fig. 8). For this XPT scenario, no baffled case is available with closely matched dr_{X2} and core density.

These findings reveal clear reduction in heat fluxes at the target individually by the ADCs and the baffles compared to the unbaffled SN. They also indicate that the impact of ADCs is stronger here than baffling in terms of the target heat flux reduction. When these two means are combined in the baffled XD, it leads to remarkably low $q_{||,OSP}^{peak}$.

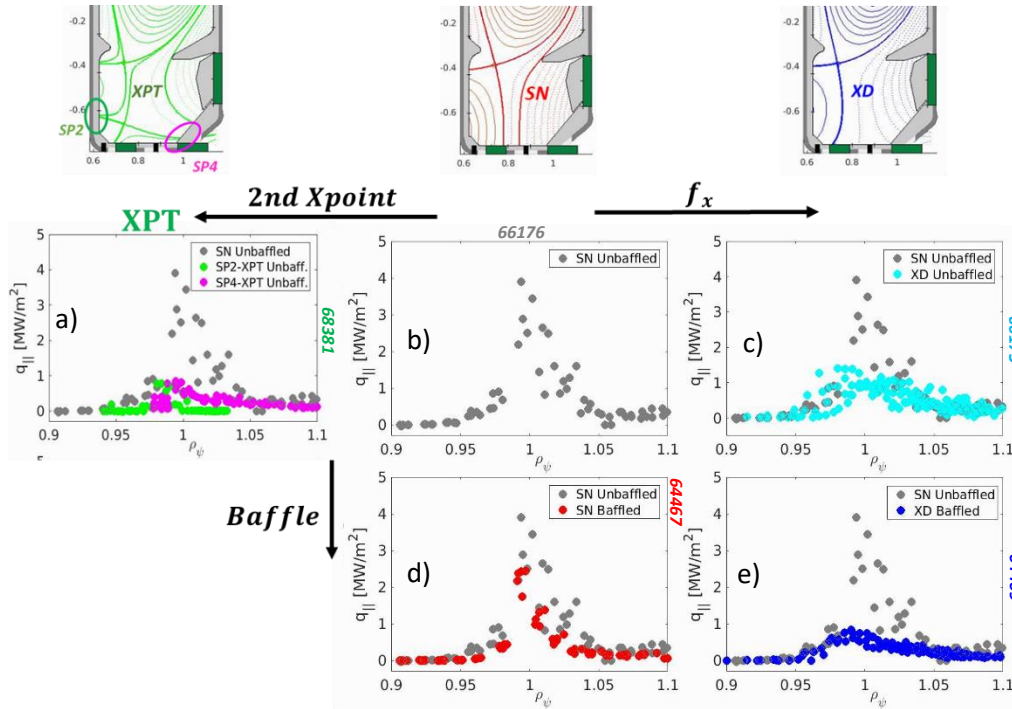


Figure 10: Plots showing radial profile of $q_{||,OSP}$ in a) Unbaffled XPT, b) Unbaffled SN, c) Unbaffled XD, d) Baffled SN and e) Baffled XD in $P_{NBI} = 0.75 \text{ MW}$ shots.

Although at these low powers ($P_{NBI} = 0.75 \text{ MW}$), the ADCs and the SN plasmas exhibit clear signs of detachment after N2 seeding i.e., a sharp reduction in J_{sat} and swift migration of the CIII front to the X-point, it was difficult to assess the effect of geometry on heat flux mitigation in the detached H-mode due to very low $q_{||,OSP}^{peak} (< 0.4 \text{ MW/m}^2)$ in detached baffled ADCs, that limits LP data interpretation. In the following section, we look at target heat fluxes in the high-power ($P_{NBI} = 1.3 \text{ MW}$) for both attached and detached ADCs.

5.2 Detachment in high power, baffled, H-mode ADCs

$q_{||,OSP}^{peak}$ is, as expected, higher in the high-power baffled SN plasmas ($\sim 5 \text{ MW/m}^2$) than the lower power baffled SN ($\sim 3 \text{ MW/m}^2$). This facilitates a reliable comparison of the detached phases. Figure 11 plots the radial profiles of $q_{||,OSP}$ for the SN and the ADCs with baffles in the attached (black) and detached (color) phases.

When attached, the $q_{\parallel,OSP}^{peak}$ in the XD remains $\sim 50\%$ lower than in SN, whereas in the XPT, $q_{\parallel,OSP}^{peak}$ is $\sim 65\%$ and $\sim 80\%$ lower at the SP2 and SP4, respectively. This agrees with our

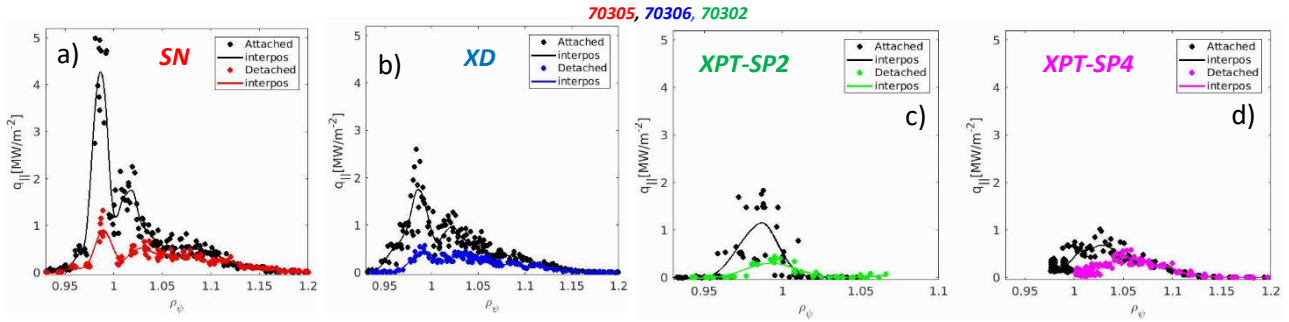


Figure 11: Plots showing radial profile of $q_{\parallel,OSP}$ in baffled a) SN, b) XD c) SP2-XPT and d) SP4-XPT in $P_{NBI} = 1.3$ MW shots.

findings at lower power. The difference in $q_{\parallel,OSP}^{peak}$ between SP2 and SP4 may be attributed to a slightly higher dr_{X2} (2-3 mm) compared to dr_{X2} (1-2 mm) in low-power XPT (fig 10a), where SP2 and SP4 show similar peak heat fluxes.

Next, we consider the heat flux mitigation with ADCs in the detached phase. Coloured profiles in fig. 11 are taken from a stable detached time window (~ 1.6 s) when the J_{sat} is at its minimum, the CIII front is at the X-point, and $H_{98} \sim 1$. An almost 80% reduction in $q_{\parallel,OSP}^{peak}$ is seen with detachment in the SN and the XD. Maximum reduction in the $q_{\parallel,OSP}$ occurs close to the strike point for $0.95 < \rho_{\psi} < 1.05$. The resulting $q_{\parallel,OSP}^{peak}$ in the XD is $\sim 60\%$ lower than the SN in the detached phase. In the XPT, $q_{\parallel,OSP}^{peak}$ is reduced by $\sim 70\%$ at SP2, but only by $\sim 40\%$ at SP4. Nevertheless, $q_{\parallel,OSP}^{peak}$ at both SP2 and SP4 remains considerably lower ($\sim 50\%$) than for the detached SN. Also, despite higher dr_{Xpt} (~ 3 mm) in detached phase, $q_{\parallel,OSP}^{peak}$ at SP2 and SP4 are similar. This may indicate that exhaust performance of detached XPT has weaker dependence on dr_{Xpt} , unlike attached XPT (fig 9), but further experiments are needed to confirm this.

Overall, we find that the improved heat flux mitigation capabilities of ADCs persist in the detached ELMy H-mode regime. Remarkably lower $q_{\parallel,OSP}^{peak}$ in detached H-mode ADCs, in addition to lower J_{sat}^{peak} and Γ_{ion} , while maintaining high core confinement (as discussed earlier), make both ADCs desirable candidates for detached H-mode operation in future tokamaks. While we see the improved heat flux mitigation at the OSP/OSPs in ADCs, it is also important to investigate the effect of ADCs at the inner strike-point (ISP), in case the missing heat-flux isn't simply diverted to the ISP. This is addressed in the following section.

5.3 Heat fluxes at the ISP

Figure 12 shows the radial profiles of the inter-ELM parallel heat fluxes at the ISP ($q_{\parallel,ISP}$) for the SN and the ADCs with baffles in the attached (black) and detached (color) phase. These profiles are taken from the same shots and time windows as in fig.11. In the attached phase, the peak $q_{\parallel,ISP}$ ($q_{\parallel,ISP}^{peak}$) is found to be over 2 times higher than at the OSP in the SN as well as the ADCs. $q_{\parallel,ISP}^{peak}$ in the ADCs remains lower than in the SN. The XPT exhibits the lowest

$q_{||,ISP}^{peak}$, i.e., $\sim 50\%$ lower than in the SN's attached phase. Earlier detachment experiments in L-mode indicated that the ISP is harder to detach in TCV [15], which is also the case here. With N_2 seeding, the XD shows the highest ($\sim 80\%$) reduction in $q_{||,ISP}^{peak}$, followed by the SN ($\sim 65\%$).

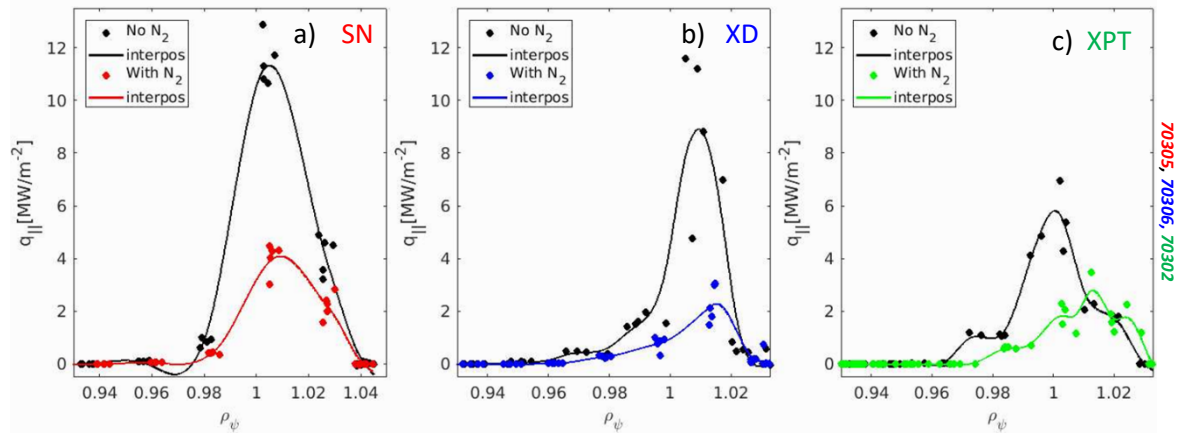


Figure 12: Plots showing radial profile of $q_{||,ISP}$ in baffled a) SN, b) XD, and c) XPT before (black) and after N_2 seeding (coloured) in $P_{NBI} = 1.3$ MW shots.

The weakest effect of N_2 seeding is observed in the XPT with only a $\sim 50\%$ reduction in the $q_{||,ISP}^{peak}$. Nonetheless, the $q_{||,ISP}^{peak}$ in both ADCs remains lower than the SN, particularly in the XD. This evidence, again, reinforces the benefits of ADCs over SN.

It can be concluded from these results that the decrease in $q_{||,OSP}$ for ADCs is not related to a redirection of power to the ISP. The effect of ADCs on different power loss channels in attached and detached H-mode will be discussed in the following section.

6 Effect of geometry on power distribution

The main power loss channels in these H-mode plasmas, apart from the previously discussed inter-ELM target heat fluxes, are impurity and hydrogenic radiation and heat pulses from ELMs. To understand the underlying mechanism leading to improved target inter-ELM heat flux mitigation in the ADCs, power loss through different channels is studied and discussed in this section.

6.1 Radiated power distribution in different geometries

Radiation emission profiles are studied using the newly upgraded RADCAM system in TCV [60]. Figure 13 plots the 2D emissivity profiles (filtered to remove ELM times) for detached H-mode for the SN and the ADCs with high power (1.3 MW). A strong radiation region localized near the X-point in all the geometries suggests we are in, or close to, X-point radiator regimes, like those observed in impurity seeding experiments in AUG [64]. Throughout, radiation is peaked around the X-point during the H-mode. However, unlike extreme X-point radiator regimes in AUG, ELMs are active in these discharges as noted earlier. These 2D profiles do not indicate that there is any remarkable influence of geometry on radiation. For a better comparison, the radiation from different regions in the vessel volume, namely core, divertor, and X-point (marked in fig. 13a) were calculated by integrating their emissivity. Figure 14 shows the radiated power from these regions together with that in the total vessel

volume. The total radiated power in the ADCs and the SN are quite similar in both the attached and detached H-mode phases. In the attached phase, the total radiated power (P_{rad}) is ~ 0.6

N2 seeded detached phase

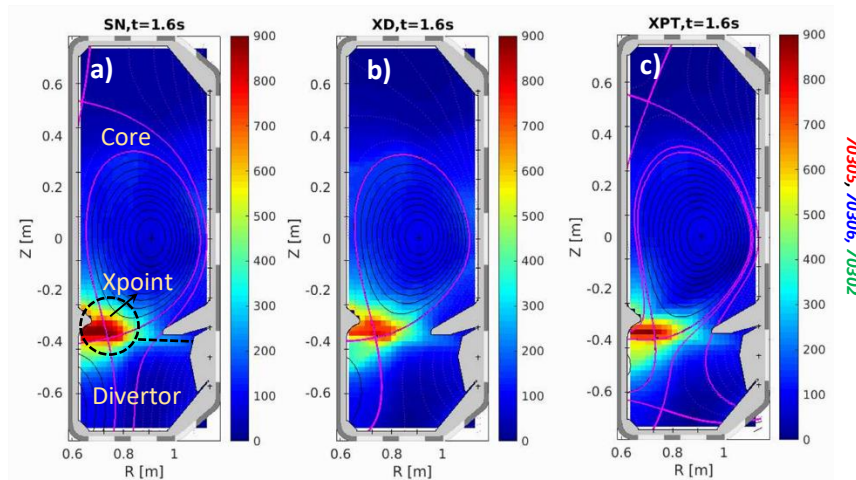


Figure 13: Plot showing 2D emissivity profiles from bolometry in baffled a) SN, b) XD, and c) XPT in $P_{NBI} = 1.3$ MW shots during the detached phase.

MW in all geometries. After the N2 seeding, P_{rad} increases to $\sim 0.75-0.8$ MW i.e $\sim 85\%$ of the total power coupled to the plasma in these geometries. The radiated power in the core and the X-point region follow a similar trend. Before the N2 seeding, the radiated power from the X-point and the divertor regions are similar, ~ 0.15 MW in ADCs and the SN. With N2 seeding, radiation from the divertor starts to decrease marginally whereas radiation from the X-point

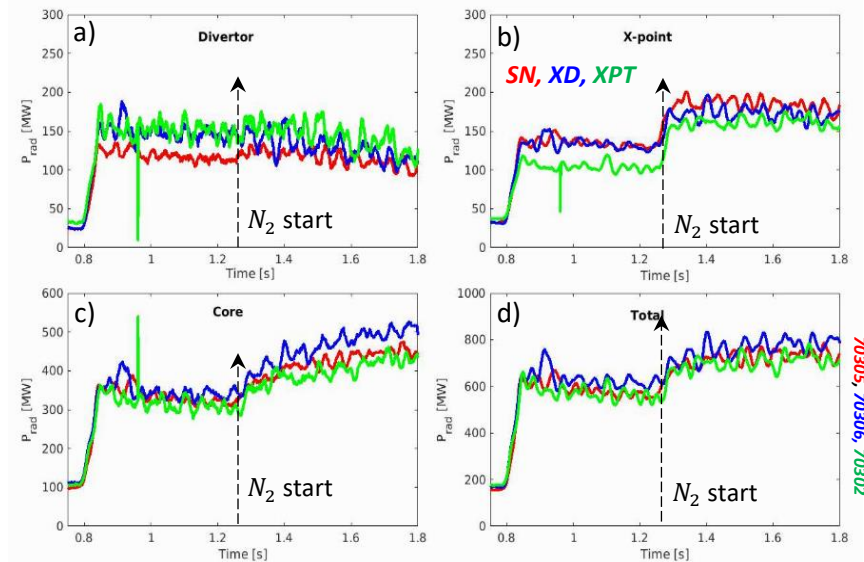


Figure 14: Plots showing the time evolution of radiated power from a) divertor, b) X-point, c) core, and d) total vessel volume in SN (red), XD (blue) and XPT (green) in $P_{NBI} = 1.3$ MW shots.

increases in all geometries. In the detached phase, the radiated power from the X-point is 40% higher than in the divertor region. However, no strong difference in radiated power nor its distribution is observed between the ADCs and the SN that could immediately explain the improved target heat flux mitigation in the ADCs. Similar results were also observed in the low power ADCs and SN.

The effect of baffles on radiation in these discharges is similar to that reported in Ref. [38].

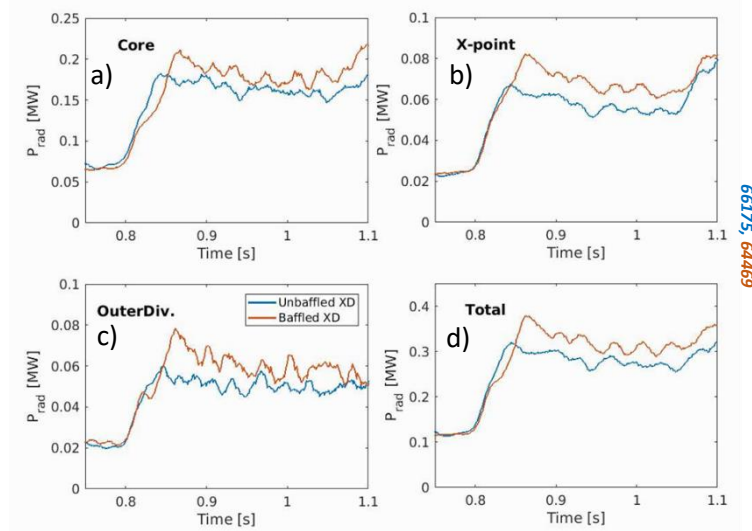


Figure 15 : Plots showing the time evolution of radiated power from a) divertor, b) X-point, c) core, and d) total vessel volume in unbaffled (blue) and baffled (orange) XD in $P_{NBI} = 0.75$ MW shots.

The baffled plasmas for all geometries exhibit higher radiated power as compared to the unbaffled plasma. Figure 15 shows the radiated power from the different regions of a baffled and an unbaffled XD plasma (0.75 MW). Increase in radiated power with baffles was observed in both ADCs and the SN. This is qualitatively consistent with the observed lower heat fluxes in the baffled scenarios.

The reason behind a reduced target heat flux in the ADCs compared to the SN could not be deduced from the radiated power analysis. An attempt to understand the power balance in the ADCs and the SN is made in the following section.

6.2 Power balance in SN and ADCs

The power balance in these H-mode plasmas is written as:

$P_{in} = P_{rad} + P_{target} + P_{ELM}$ where P_{in} is the ohmic and NBI power delivered to the plasma after accounting for beam duct and orbit losses, calculated using the ASTRA code [65]. P_{target} is the total inter-ELM power deposited on the divertor and is calculated by integrating the inter-ELM heat flux across all the strike points, assuming toroidal symmetry [51]. P_{rad} is the total radiated power and P_{ELM} is the power loss due to the ELMs. Figure 16 shows the time evolution of P_{in} , P_{rad} , P_{target} and P_{ELM} for the ADCs and the SN for the 1.3 MW baffled scenarios from fig 2. Both the ADCs and the SN have similar power distributions in terms of P_{in} , P_{rad} and P_{ELM} in the attached and detached H-mode. We find P_{ELM} comparable to P_{target} for all geometries. The effect of divertor geometry is evident only for P_{target} . This highlights also that the effect of divertor geometry on the peak inter-ELM heat fluxes at the SPs is more pronounced (as discussed in sec.5) than on the total power deposited at the SPs, particularly in the detached phase.

The power deposited at the divertor target is, clearly, only a small fraction i.e., $\leq 20\%$ of the total radiated power. The total radiated power accounts for $\sim 60\%$ and 85% of the P_{in} in the attached and detached phases, respectively. The absolute difference in P_{target} between

geometries is relatively small within the level of fluctuation in the total P_{rad} data. Nevertheless, the XD geometry exhibits slightly higher radiated power throughout the attached and the detached phases. Similar trends were also observed in lower power plasmas. This small but consistent difference in radiated power could explain, at least in part, the reduced target heat

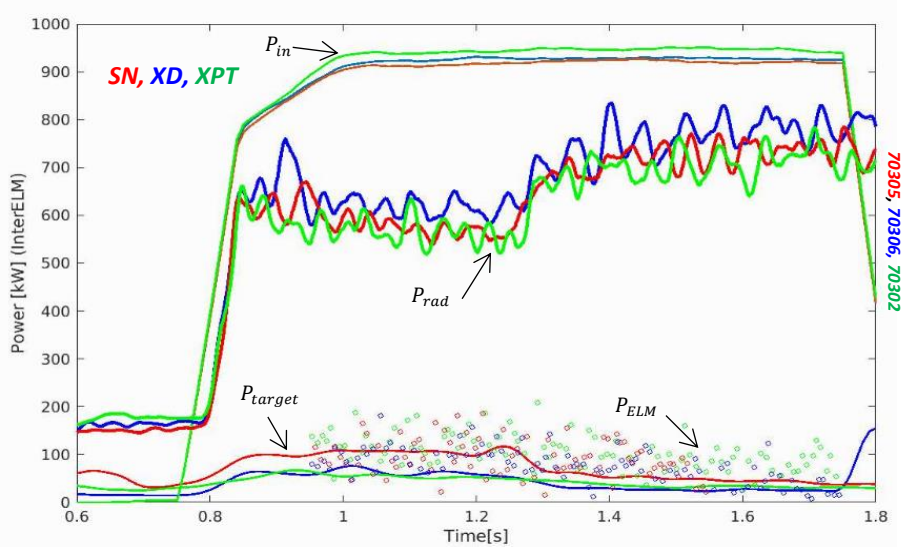


Figure 16: Plot showing power distribution in baffled SN (red), XD (blue) and XPT (green) in $P_{NBI} = 1.3$ MW shots.

flux in the XD plasmas.

These results suggest that even in discharges with high radiated power fractions and radiation localised around the X-point, the divertor leg geometry still influences the target heat fluxes. The physics behind this heat flux reduction remain unclear. It might be due to the differences in radial transport in ADCs leading to the reduction in the peak heat fluxes. Power loss due to non-coronal processes, which are predicted to be enhanced in baffled XD, might also be responsible for this reduction [51]. Another possibility can be the difference in neutral losses, which can be enhanced in the XD [47].

7. Conclusions

High confinement detached H-mode ADCs, namely X-Divertor (XD) and X-Point Target (XPT), with improved heat and particle flux mitigation at the outer target, have been achieved with N_2 seeding at TCV. A detailed comparative study of many core and target parameters between the ADCs (XD and XPT) and the Single-null (SN) has been presented in this paper. The benefits of baffles, as reported in earlier experiments [38], are reproduced in all geometries. Compared to the baffled SN, a remarkable decrease in inter-ELM $q_{||,OSP}^{peak}$ ($>50\%$) and J_{sat}^{peak} is achieved in ADCs for both attached and detached phases, whilst maintaining high core confinement $H_{98} \geq 1$. Figure 16 shows a simplified summary of the effect of adding baffles, modifying geometry and N_2 seeded detachment, respectively. Compared to an unbaffled, attached SN, $\sim 95\%$ - 98% reduction in $q_{||,OSP}^{peak}$ is achieved as a synergistic effect of adding baffles, modifying the divertor geometry and impurity seeded detachment. We have shown that the reduction in $q_{||,OSP}^{peak}$ is not a redistribution of $q_{||}$ between outer and inner strike points in the

ADCs, with the $q_{||}^{peak}$ at the inner target also lower in the ADCs. The power distribution analysis indicates marginally higher radiated power in the XD, however, the physics behind

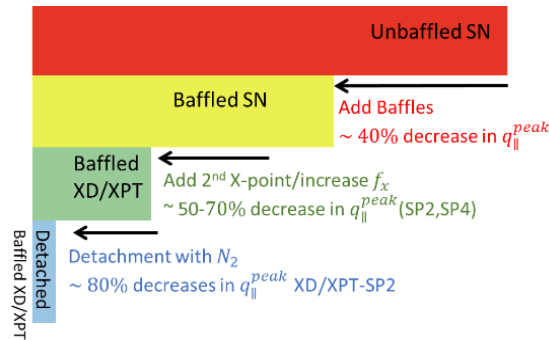


Figure17: Schematic summarising the effect of adding baffle, modifying divertor geometry and impurity seeded detachment on $q_{||,OSP}^{peak}$

the reduced particle/heat flux to the target in ADCs remains unclear. These results exhibit a promising potential of XD and XPT in future reactors motivating continued investigation of these geometries.

In future, we plan to expand the ADCs in TCV even experiments to higher power scenarios with combined NBI and ECRH heating. The advantages of ADCs will be assessed in further operational regimes such as small ELM scenarios. Initial results from ADC experiments in such small-ELM regimes support the results in this paper. Experiments with increased poloidally and toroidally distributed impurity seeding uniformity (multiple gas injection points) in ADCs are also being developed, to seek optimisation of the impurity injection in TCV. Efforts are also continued to initiate numerical modelling of these ADCs in TCV, which is thought to be instrumental in understanding the underlying physics behind the improved exhaust performance of ADCs.

8. Acknowledgement

This work was supported in part by the Swiss National Science Foundation. This work has been carried out within the framework of the EUROfusion Consortium, funded by the European Union via the Euratom Research and Training Programme (Grant Agreement No 101052200 — EUROfusion). Views and opinions expressed are however those of the author(s) only and do not necessarily reflect those of the European Union or the European Commission. Neither the European Union nor the European Commission can be held responsible for them.

9. References

- [1] Pitts R A et al 2019 Physics basis for the first ITER tungsten divertor *Nuclear Materials and Energy* **20** 100696
- [2] Zohm H et al 2013 On the physics guidelines for a tokamak DEMO *Nuclear Fusion* **53** 073019
- [3] Wischmeier M 2015 High density operation for reactor-relevant power exhaust *Journal of Nuclear Materials* **463** 22–9

- [4] Krasheninnikov S I, Kukushkin A S and Pshenov A A 2016 Divertor plasma detachment *Physics of Plasmas* **23** 055602
- [5] Leonard A W 2018 Plasma detachment in divertor tokamaks *Plasma Physics and Controlled Fusion* **60** 044001
- [6] Stangeby P C 2000 *The plasma boundary of magnetic fusion devices* (Bristol: Institute of Physics Publishing)
- [7] Lipschultz B et al 2007 Divertor physics research on alcator C-Mod *Fusion Sci. Technol.* **51** 369–89
- [8] Verhaegh K et al 2017 Spectroscopic investigations of divertor detachment in TCV *Nuclear Materials and Energy* **12** 1112-1117
- [9] Potzel S et al A 2014 A new experimental classification of divertor detachment in ASDEX Upgrade *Nucl. Fusion* **54** 013001
- [10] Stangeby P C and Leonard A W 2011 Obtaining reactor-relevant divertor conditions in tokamaks *Nucl. Fusion* **51** 063001
- [11] Kallenbach A et al 2013 Impurity seeding for tokamak power exhaust: From present devices via ITER to DEMO *Plasma Phys. Control. Fusion* **55** 124041
- [12] Hosogane N et al 1992 Plasma-surface interactions in controlled fusion devices *J. Nucl. Mater.* **196–198** 750–4
- [13] Reimerdes H et al 2017 TCV experiments towards the development of a plasma exhaust solution *Nucl. Fusion* **57** 126007
- [14] Petrie T W et al 1997 Radiative divertor experiments in DIII-D with D2 injection *Nucl. Fusion* **37** 321–38
- [15] Février O et al 2020 Nitrogen-seeded divertor detachment in TCV L-mode plasmas *Plasma Physics and Controlled Fusion* **62** 035017
- [16] Asakura N et al 2009 Investigations of impurity seeding and radiation control for long-pulse and high-density H-mode plasmas in JT-60U *Nucl. Fusion* **49** 115010
- [17] Dunne M G et al 2017 The role of the density profile in the ASDEX-Upgrade pedestal structure *Plasma Phys. Control. Fusion* **59** 014017
- [18] Greenwald M, Terry J L, Wolfe S M, Neilson G H, Zweibellben M G, Kaye S M and Neilson G H 1988 A new look at density limits in tokamaks *Nucl. Fusion* **28** 2199
- [19] Kallenbach A et al 2015 Partial detachment of high-power discharges in ASDEX upgrade *Nucl. Fusion* **55** 053026
- [20] G.F. Matthews *et al* 1999 Studies in JET divertors of varied geometry. II: Impurity seeded plasmas *Nucl. Fusion* **39** 19
- [21] Gruber O et al 1995 Observation of continuous divertor detachment in H-mode discharges in ASDEX upgrade *Phys. Rev. Lett.* **74** 4217

- [22] Leonard A Wet et al 2015 Compatibility of detached divertor operation with robust edge pedestal performance *J. Nucl. Mater.* **463** 519
- [23] Kukushkin A S et al 2013 Consequences of a reduction of the upstream power SOL width in ITER *J. Nucl. Mater.* **438** S203–7
- [24] Pitts R A et al 2013 A full tungsten divertor for ITER: Physics issues and design status *J. Nucl. Mater.* **438** S48–56
- [25] Wang L et al 2021 Integration of full divertor detachment with improved core confinement for tokamak fusion plasmas *Nature Communications* 2021 12:1 **12** 1–9
- [26] Bernert M et al 2021 X-point radiation, its control and an ELM suppressed radiating regime at the ASDEX Upgrade tokamak *Nuclear Fusion* **61** 024001
- [27] Loarte A et al 2007 Chapter 4: Power and particle control *Nucl. Fusion* **47** S203
- [28] Zohm H et al 2021 The EU strategy for solving the DEMO exhaust problem *Fusion Engineering and Design* **166** 112307
- [29] Asakura N et al 2017 Studies of power exhaust and divertor design for a 1.5 GW-level fusion power DEMO *Nuclear Fusion* **57** 126050
- [30] Bachmann C et al 2019 Critical design issues in DEMO and solution strategies *Fusion Engineering and Design* **146** 178–81
- [31] Reimerdes H et al 2020 Assessment of alternative divertor configurations as an exhaust solution for DEMO *Nuclear Fusion* **60** 066030
- [32] Militello F. et al 2021 Preliminary analysis of alternative divertors for DEMO *Nucl. Mater. Energy* **26** 100908
- [33] Reimerdes H et al 2016 TCV divertor upgrade for alternative magnetic configurations *Nucl. Mater. Energy* **12** 1106-1111
- [34] Theiler C et al 2017 Results from recent detachment experiments in alternative divertor configurations on TCV *Nuclear Fusion* **57** 072008
- [35] Petrie T W et al 2013 Effect of changes in separatrix magnetic geometry on divertor behaviour in DIII-D *Nucl. Fusion* **53** 113024
- [36] Rindt P et al 2021 Conceptual design of a liquid-metal divertor for the European DEMO *Fusion Engineering and Design* **173** 112812
- [37] Pitcher C S et al 2000 The effect of divertor baffling on Alcator C-Mod discharges *Physics of Plasmas* **7** 1894–903
- [38] Février O et al 2021 Divertor closure effects on the TCV boundary plasma *Nuclear Materials and Energy* **27** 100977
- [39] Kotschenreuther M, Valanju P, Covele B and Mahajan S 2013 Magnetic geometry and physics of advanced divertors: The X-divertor and the snowflake *Phys. Plasmas* **20** 102507

- [40] Covele B, Valanju P, Kotschenreuther M and Mahajan S 2014 An exploration of advanced X-divertor scenarios on ITER *Nucl. Fusion* **54** 072006
- [41] Covele B et al 2017 Increased heat dissipation with the X-divertor geometry facilitating detachment onset at lower density in DIII-D *Nuclear Fusion* **57** 086017
- [42] LaBombard B et al 2015 ADX: A high field, high power density, advanced divertor and RF tokamak *Nucl. Fusion* **55** 053020
- [43] Valanju P M, Kotschenreuther M, Mahajan S M and Canik J 2009 Super-X divertors and high power density fusion devices *Phys. Plasmas* **16** 056110
- [44] Labit B. et al 2016 Experimental studies of the snowflake divertor in TCV *Nucl. Mater. Energy* **12** 1015-1019
- [45] Vijvers W A J et al 2014 Power exhaust in the snowflake divertor for L- and H-mode TCV tokamak plasmas *Nucl. Fusion* **54** 023009
- [46] Coda S. et al 2017 Overview of the TCV tokamak program: Scientific progress and facility upgrades *Nucl. Fusion* **57** 102011
- [47] Pitts R A et al 2001 Divertor geometry effects on detachment in TCV *J. Nucl. Mater.* **290** 940–6
- [48] Reimerdes H et al 2013 Power distribution in the snowflake divertor in TCV *Plasma Phys. Control. Fusion* **55** 124027
- [49] Harrison J R et al 2017 Detachment evolution on the TCV tokamak *Nucl. Mater. Energy* **12** 1071-1076
- [50] Chen Z P et al 2020 SOLPS-ITER modeling of boosted carbon radiation through non-coronal effects in an X-divertor facilitating detachment in DIII-D *Nuclear Fusion* **60** 046005
- [51] Harrison J R et al 2019 Progress toward divertor detachment on TCV within H-mode operating parameters *Plasma Phys. Control. Fusion* **61** 065024
- [52] Fasoli A et al 2015 TCV heating and in-vessel upgrades for addressing DEMO physics issues *Nucl. Fusion* **55** 043006
- [53] Sheikh U A et al 2021 Impact of the new TCV baffled divertor upgrade on pedestal structure and performance *Nuclear Materials and Energy* **26** 100933
- [54] Ambrosino R 2021 DTT - Divertor Tokamak Test facility: A testbed for DEMO *Fusion Engineering and Design* **167** 112330
- [55] Reimerdes H et al 2022 Overview of the TCV tokamak experimental programme *Nuclear Fusion* **62** 42018
- [56] Hawke J et al 2017 Improving spatial and spectral resolution of TCV Thomson scattering *J. Instrum.* **12** C12005
- [57] Février O et al 2018 Analysis of wall-embedded Langmuir probe signals in different conditions on the Tokamak à Configuration Variable *Rev. Sci. Instrum.* **89** 053502

- [58] de Oliveira H, Marmillod P, Theiler C, Chavan R, Février O, Labit B, Lavanchy P, Marlétaz B and Pitts R A 2019 Langmuir probe electronics upgrade on the tokamak à configuration variable *Rev. Sci. Instrum.* **90** 083502
- [59] Kamleitner J 2015 Suprathermal electron studies in tokamak plasmas by means of diagnostic measurements and modelling, *PhD Thesis EPFL*.
- [60] Perek A 2019 MANTIS: A real-time quantitative multispectral imaging system for fusion plasmas *Rev. Sci. Instrumen.* **90** 123514
- [61] Wagner F 2009 The physics basis of ITER confinement *AIP Conference Proceedings* **31** 1095
- [62] ITER-Physics-Basis: Chapter-2, *Nucl. Fusion* **39**, 2175 (1999).
- [63] Ravensbergen T et al 2021 Real-time feedback control of the impurity emission front in tokamak divertor plasmas *Nature Communications* **12** 1105
- [64] Sheikh U. et al *In preperation*
- [65] Pereverzev G V., and Yushmanov, P. N 2002 ASTRA Automated system for transport analysis in a tokamak *IPP--5-98* 147